Applied Catalysis B: Environment and Energy 383 (2026) 126068

Contents lists available at ScienceDirect

Applied Catalysis B: Environment and Energy

journal homepage: www.elsevier.com/locate/apcatb

Efficient CO electrosynthesis in hydroxide-mediated reactive capture systems through catalyst and microenvironment design

Cheng Wang [a,b,1], Manman Qi [c,1], Zhi Zheng [a], Xiaobo Zheng [d], Shuai Li [b], Peng Li [e], Tianyi Ma [e], Bernt Johannessen [f], Yitong Cao [g], Jiabao Yi [g], Hai Yu [b,*], Jie Zeng [a,h,**], Yong Zhao [b,g,***]

[a] Hefei National Research Center for Physical Sciences at the Microscale, Key Laboratory of Strongly-Coupled Quantum Matter Physics of Chinese Academy of Sciences, Key Laboratory of Surface and Interface Chemistry and Energy Catalysis of Anhui Higher Education Institutes, Department of Chemical Physics, University of Science and Technology of China, Hefei, Anhui 230026, PR China
[b] CSIRO Energy Center, 10 Murray Dwyer Cc, Mayfield West, NSW 2304, Australia
[c] Department of Chemical and Biomolecular Engineering, University of Delaware, Newark, DE, USA
[d] Center for Clean Energy Technology, School of Mathematical and Physical Sciences, Faculty of Science, University of Technology Sydney, Sydney, NSW 2007, Australia
[e] School of Science, RMIT University, Melbourne, VIC 3000, Australia
[f] Australian Synchrotron, ANSTO, 800 Blackburn Road, Clayton, VIC 3168, Australia
[g] Global Innovative Center of Advanced Nanomaterials, School of Engineering, University of Newcastle, University Drive, Callaghan, NSW 2308, Australia
[h] School of Chemistry & Chemical Engineering, Anhui University of Technology, Ma'anshan, Anhui 243002, PR China

ARTICLE INFO

Keywords:
Ni single-atom catalyst
CO_2 reduction
Reactive capture
CO_2 regeneration
Microenvironment control

ABSTRACT

The electrochemical conversion of captured CO_2 – also known as reactive capture – offers a promising approach to produce renewable carbon monoxide (CO) while bypass the energy and cost-intensive CO_2 capture, purification and pressurization processes at large scale. However, current reactive capture systems suffer from low CO selectivity (< 50 %) and productivity (< 100 mA cm^{-2}) due to the lack of efficient electrocatalysts and limited CO_2 availability at the reactive interfaces. Here, we develop a coupled catalyst and microenvironment strategy to overcome these barriers. Employing Ni single-atom catalysts with a high density of reactive sites (Ni loading up to 3.0 wt%), together with enhanced CO_2 regeneration and transport to the catalyst via local hydrophobicity control, we achieved efficient CO production with a Faradaic efficiency of 68 % at 100 mA cm^{-2} with stable performance maintained over 100 h in a hydroxide-mediated reactive capture system. The system achieved a CO energy efficiency of 27 % and an energy intensity of 37.7 GJ ton^{-1}_{CO}, outperforming the best reported amine- and hydroxide-based reactive capture processes operating at ambient temperature and pressure.

1. Introduction

Electrochemical CO_2 reduction (CO_2R) powered by renewable electricity is promising to convert CO_2 waste into chemical feedstocks and fuels offering a pathway to achieve net-zero emission [1–3]. Carbon monoxide (CO), as one of the most readily reduced CO_2R products, is particularly attractive due to its high market demand and wide applications in industry such as the production of synthetic fuels and metal refining [4–8]. However, conventional CO_2R-to-CO requires pure CO_2 supply to achieve considerable reaction rate and CO product selectivity. The energy- and capital-intensive CO_2 capture, regeneration and purification to produce pressurized CO_2 hinders the practical applications of this technology [9–11].

Direct conversion of CO_2 capture solution, also known as reactive capture (Fig. 1a), avoids the energy-intensive CO_2 regeneration and purification, representing a promising way to achieve a large-scale CO_2-

* Corresponding author.
** Corresponding author at: Hefei National Research Center for Physical Sciences at the Microscale, Key Laboratory of Strongly-Coupled Quantum Matter Physics of Chinese Academy of Sciences, Key Laboratory of Surface and Interface Chemistry and Energy Catalysis of Anhui Higher Education Institutes, Department of Chemical Physics, University of Science and Technology of China, Hefei, Anhui 230026, PR China.
*** Corresponding author at: CSIRO Energy Center, 10 Murray Dwyer Cc, Mayfield West, NSW 2304, Australia.
E-mail addresses: hai.yu@csiro.au (H. Yu), zengj@ustc.edu.cn (J. Zeng), yong.zhao@newcastle.edu.au (Y. Zhao).
[1] These authors contributed equally.

https://doi.org/10.1016/j.apcatb.2025.126068
Received 3 August 2025; Received in revised form 19 September 2025; Accepted 10 October 2025
Available online 11 October 2025

to-CO conversion [12–14]. Current reactive capture systems rely on organic amine or aqueous hydroxide solution to carry CO_2 to the catalyst surface [15–21]. Despite their high CO_2 adsorption capacity (up to 0.57 mol CO_2/mol_{amine}), these reagents capture CO_2 in the form of carbamates or carbonates which are thermodynamically stable and difficult to be activated in the solution-mediated electrochemical process [21–25]. The dominant reactive species is the dissolved CO_2 gas with a solubility of tens of millimolar [26,27]. The lack of reactive CO_2 species near catalyst surface limits the reaction rates and selectivity for CO production (e.g., CO Faradaic efficiency < 30 % at 100 mA cm^{-2}) [15].

Enabling gaseous CO_2 regeneration in the vicinity of catalyst via pH swing is an approach to improve the local CO_2 concentration. The protons electromigrated from the anode side or bipolar membrane react with the capture solution to generate CO_2 that is subsequently electrochemically reduced on the cathode. Employing the carbonate electrolyte as feedstock and silver nanoparticles as catalyst has resulted in a CO Faradaic efficiency (FE) of 47 % at 100 mA cm^{-2} [21]. Employing a single-atom Ni catalyst embedded in N-doped carbon (Ni-N-C) in the MEA-based reactive capture system promoted the CO FE to 65 % yet at a lower current density of 50 mA cm^{-2} [17]. However, the CO selectivity at industrially relevant current densities (e.g., 200 mA cm^{-2}) in these reactive capture systems is still largely constrained (FE_{CO} < 50 %) due to various entangled factors such as the low intrinsic activity of catalysts and limited CO_2 transport to catalyst [28–32]. The limited electrocatalytic performances challenge the practical applications of this integrated carbon capture and utilization technology. Improvements on both catalyst activity and CO_2 availability are required to promote the CO_2R kinetics while suppressing the competing proton reduction for an improved CO selectivity at the desired reaction rates (> 100 mA cm^{-2}).

Herein, we report a systematic catalyst and catalyst microenvironment engineering to improve CO production at industrially desirable current densities in a KOH-based reactive capture system (Fig. 1b). We employ a Ni single-atom catalyst (Ni-SAC) embedded in N-doped carbons, which possess high intrinsic activity for CO_2R and sluggish kinetics for hydrogen evolution reaction (HER). To boost the reaction rate, we develop a Ni-SAC with a remarkably high density of active sites where the Ni single-atom loading reaches 3 wt%. We further improve the regeneration and transport of CO_2 to the catalyst surface via catalyst microenvironment control. Employing this systematic catalyst strategy, we achieved a high CO Faradaic efficiency of 61 % at 200 mA cm^{-2} together with a CO_2 utilization efficiency of 89 %, surpassing the results in all the prior reactive capture systems (Table S1).

2. Experimental

2.1. Chemicals and materials

Zinc(II) nitrate hexahydrate ($Zn(NO_3)_2{\cdot}6\ H_2O$), methanol (CH_3OH), 2-methylimidazole ($C_4H_6N_2$), nickel(II) acetylacetonate ($Ni(acac)_2$), sulfuric acid (H_2SO_4), potassium hydroxide (KOH), Nafion solution (PFSA, ~5 wt%), poly(ethyleneimine) solution (PEI, ~50 wt%), polytetrafluoroethylene solution (PTFE, ~60 wt%), 1-propanesulfonic acid 3-(trimethylsilyl) sodium salt (DSS), dimethyl sulfoxide-d_6 (DMSO-d_6), and Nafion 117 membranes were obtained from Sigma-Aldrich. All reagents were used as received without further purification unless otherwise specified. Ultrapure water (18.2 MΩ cm resistivity, Millipore) was utilized for all experiments.

2.2. Preparation of catalysts and working electrodes

Synthesis of ZIF-8 was synthesized by mixing 6.78 g $Zn(NO_3)_2{\cdot}6\ H_2O$ and 7.92 g 2-methylimidazole in separate 150 mL CH_3OH solutions, followed by combination and heating at 60 °C for 24 h. The precipitate was washed with CH_3OH and vacuum-dried at 60 °C. For Ni-SAC synthesis, $Ni(acac)_2$ (20, 60, or 100 mg for Ni-SAC-1, −2, and −3,

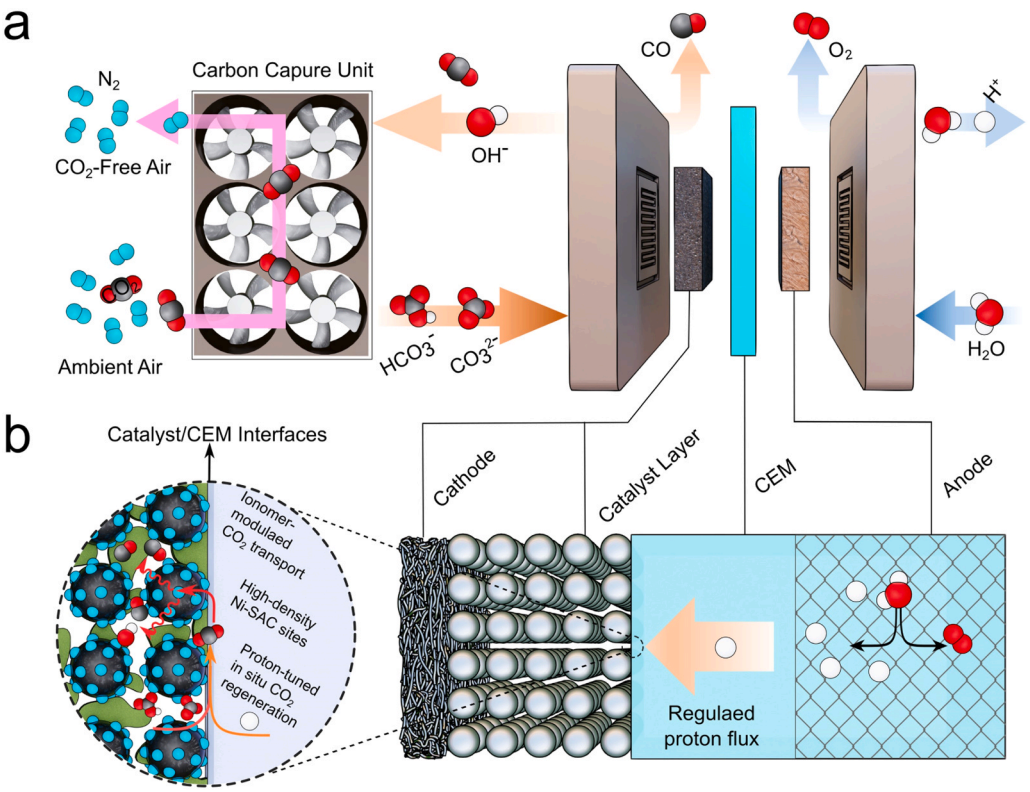

Fig. 1. Schematic illustration of a reactive capture system for CO electrosynthesis. (a) The integration of a CO_2 capture unit with an electrochemical reactor for CO_2-to-CO conversion. (b) The cross-section of the electrolyser from anode to cathode. The enlarged section shows the catalyst/cation-exchange membrane interface and the strategies employed to enhance energy efficiency of CO_2-to-CO conversion.

respectively) and 100 mg of ZIF-8 were placed upstream and downstream, respectively, in a dual-zone furnace. Under Ar flow (10 mL min^{-1}), the upstream and downstream zones were heated to 240 °C and 400 °C for 2 h, followed by downstream carbonization at 900 °C (10 °C min^{-1} ramp, 3 h dwell).

Working electrodes were prepared by dispersing 9 mg of catalyst (Ni-SAC-1, −2, or −3) in 2 mL methanol, followed by 30 min sonication. Subsequently, 30 μL of ~5 wt% Nafion solution was added and sonicated for an additional 60 min to form a homogeneous ink, which was spray-coated onto 2.5 × 2.5 cm^2 hydrophilic carbon paper (AvCarb MGL190) to achieve a loading of approximately 0.8 mg cm^{-2}. The loading was measured by weighing the carbon paper before and after air-brushing. To modulate catalyst layer (CL) thickness, 4.5, 9, and 18 mg of Ni-SAC-2 were processed similarly, yielding Ni-SAC-2 μm, −6 μm, and −8 μm electrodes. For PFSA content variation, 9 mg of Ni-SAC-2 was mixed with 15, 30, or 90 μL of ~5 wt% Nafion, generating Ni-SAC-7 %, −13 %, and −37 % PFSA electrodes. To study ionomer effects, inks with 30 μL of either PEI or PTFE solution (both ~5 wt%) were prepared with 9 mg Ni-SAC-2, producing Ni-SAC-PEI and Ni-SAC-PTFE electrodes.

2.3. Simulated CO_2 capture process

CO_2 Capture Experiments by Potassium Hydroxide (KOH) Solution. Initially, a 2 M KOH solution was prepared. Subsequently, 60 mL of the 2 M KOH solution was transferred into a glass bottle. CO_2 was then introduced into the bottle at a flow rate of 50 mL min^{-1} for 120 min to finish the CO_2 capture process. After the CO_2 capture process, the pH of the resulting solution (~9.6) was measured using a calibrated pH meter (Apera Instruments AI311, Premium Series PH60). The species present in the capture solution, as well as their concentrations, were determined based on a Vapor Liquid Equilibrium (VLE) Model [33]. The CO_2 loading capacity in 2 M KOH at pH ~9.6 is approximately 0.87 mol CO_2 per mol KOH. The details of VLE model and MATLAB code are shown in Supplementary Information.

2.4. Electrochemical measurements

The electrolysis experiments of the carbon capture solution were conducted in a 1 cm × 1 cm membrane electrode assembly (MEA) electrolyzer, featuring serpentine flow channels integrated into both the stainless-steel cathode and the titanium anode current collectors. In the experimental setup, the cathode was positioned on the cathode plate of the MEA, followed by the careful placement of a mixed cellulose ester (MCE) membrane over the cathode. A cation-exchange membrane (CEM) was then placed atop the MCE membrane, with the anode positioned on top of the membrane assembly. In all experiments, unless otherwise noted, the cathode feed was the previously prepared carbon capture solution, while the anode was supplied with 0.05 M H_2SO_4. Both catholyte and anolyte flow rate were setting at 10 mL min^{-1}. Electrochemical measurements were performed using a potentiostat (Lvium OctoStat 5000), and the full cell voltages reported were not IR-compensated unless otherwise specified. For the stability test, the MEA was operated at a constant current density of 100 mA cm^{-2}, and 2 litre of CO_2 capture solution (pH ~9.6) was prepared to ensure that the electrolyte composition remained constant during the long electrolysis process. The details of electrochemical data analysis are shown in Supplementary Information.

2.5. Material characterizations

X-ray diffraction (XRD) patterns were collected using a Bruker D8 Advance diffractometer equipped with Cu K_α radiation ($\lambda = 1.54$ Å) at a scan rate of 10° min^{-1}. Surface morphologies and cross-sectional structures were examined using a field-emission scanning electron microscope (SEM, JEOL FE7900F). High-angle annular dark-field scanning transmission electron microscopy (HAADF-STEM) and energy-dispersive X-ray (EDX) elemental mapping were conducted on a JEOL ARM-200F transmission electron microscope operating at 200 kV. Nickel loading in the catalysts was quantified via inductively coupled plasma atomic emission spectrometry (ICP-AES, PerkinElmer NexION2000). X-ray photoelectron spectroscopy (XPS) was performed on a Thermo Scientific K-Alpha+ spectrometer using an Al K_α excitation source (1486.6 eV), with binding energies calibrated against the C 1 s peak at 284.8 eV to correct for surface charging. Ni K-edge X-ray absorption spectroscopy (XAS) measurements were carried out at the 12-ID beamline of the Australian Synchrotron (ANSTO, 3.0 GeV, 200 mA), utilizing a fixed-exit Si (111) double-crystal monochromator to tune the incident X-ray energy from 2.0 to 13.6 keV. A Ni foil standard was employed for energy calibration. All XAS data were acquired in transmission mode using pellets prepared by homogenously mixing the catalyst powder with cellulose as a binder. The details of XAFS data analysis are shown in Supplementary Information.

2.6. Computational details

The details of Finite Element Method (FEM) simulation and Density Functional Theory (DFT) calculation are shown in Supplementary Information.

2.7. Energy analysis details

The details of energy analysis for gas-phase CO_2 system and CO_2 reactive capture system are shown in Supplementary Information.

3. Results and discussion

3.1. Ni-SAC synthesis and characterization

Metal single atoms embedded in nitrogen-doped carbon (M-N-C) frameworks have demonstrated exceptional activity and selectivity for CO production in gas-fed CO_2 reduction (CO_2R) systems, outperforming conventional noble metals such as Ag and Au [34–38]. In contrast, reactive capture systems suffer from a substantial deficiency of CO_2 reactant, making the suppression of the hydrogen evolution reaction (HER) critical for achieving high CO selectivity. Our density functional theory (DFT) calculations revealed that Ni–N–C exhibits the most positive difference between the limiting potentials for CO_2 reduction and HER $U_L(CO_2)$-$U_L(H_2)$ among common M-N-C catalysts (where M = Fe, Co, Zn, or Ni) (Figs. S1–S2), indicating its superior ability to promote CO_2 reduction while suppressing HER [39,40]. This highlights the intrinsic activity of Ni-N-C sites and their strong potential for application in reactive capture-based CO_2R [41–43]. Although current reactive capture systems employing Ni-N-C catalysts show promising CO selectivity, their reaction rates remain below 100 mA cm^{-2} (Faradaic efficiency ~65 % at 50 mA cm^{-2}), likely due to the low density of surface-accessible Ni single-atom active sites (typically <1 wt% Ni loading) [17,44]. To address this limitation, we aimed to enhance CO productivity by increasing the density of Ni active sites within the reactive capture system.

We synthesised the Ni single-atom catalysts (Ni-SACs) using a chemical vapour deposition (CVD) method that enables precise control over metal loading. In a typical procedure (Fig. 2a), nickel acetylacetonate powder served as the sublimation source and was placed upstream of the host material – zeolitic imidazolate framework (ZIF-8) powder – inside a horizontal quartz tube [45]. Upon heating to 240 °C, the nickel precursor sublimated into the vapour phase and deposited onto the surface of ZIF-8 nanoparticles. Subsequent pyrolysis at 900 °C caused the Ni atoms to dissociate from the acetylacetonate ligands and anchor onto the N-surrounding vacancies generated by Zn evaporation from ZIF-8 derived carbon. By varying the amount of the sublimation source, we successfully synthesised a series of Ni-SACs with Ni loadings ranging

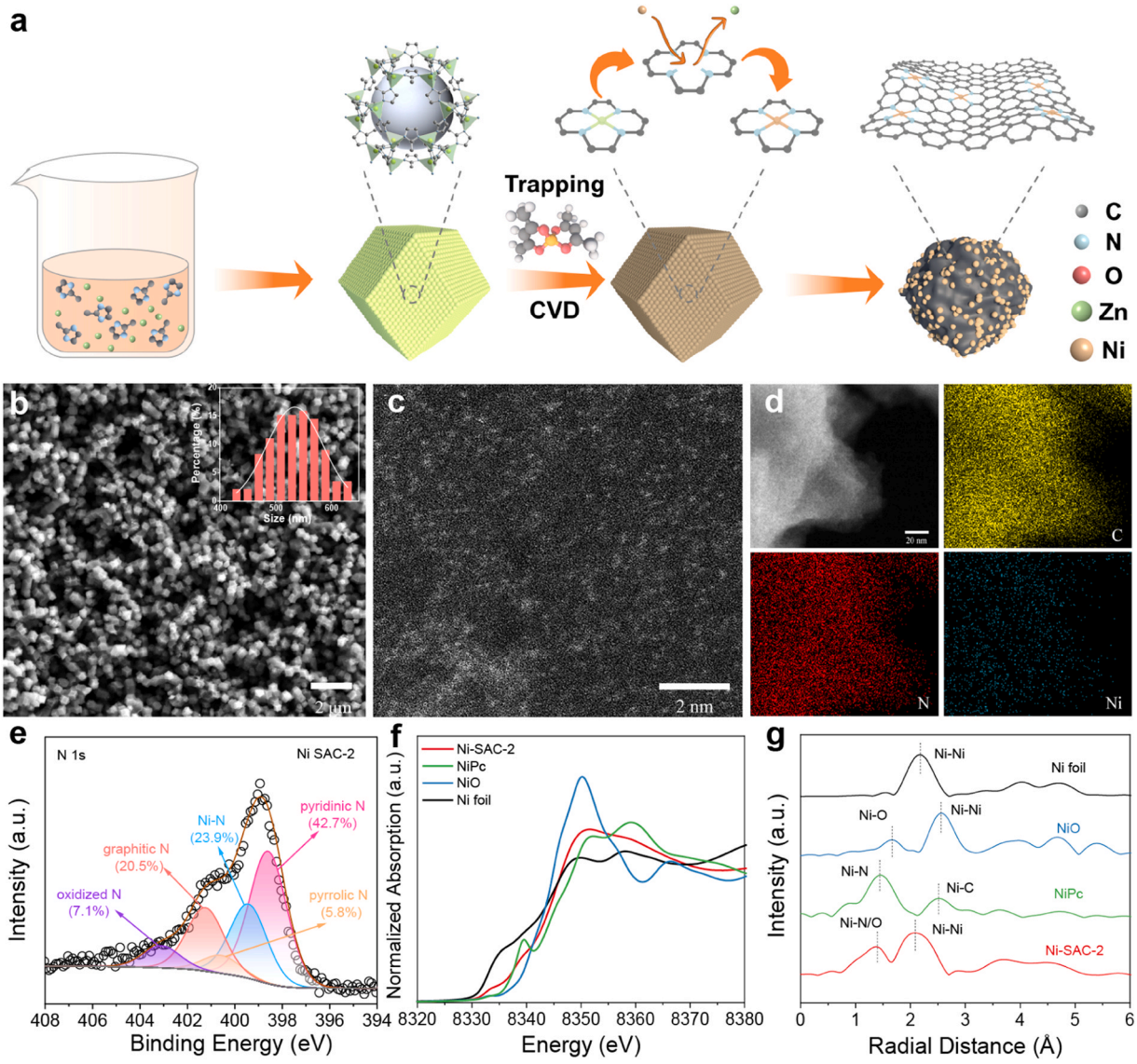

Fig. 2. Structural characterization of Ni-SAC catalysts. (a) Schematic illustration of the fabrication of Ni-SAC catalysts. (b) SEM images of Ni-SAC-2. (c) High-resolution STEM image, and (d) EDS mapping images of Ni-SAC-2. (e) High-resolution N 1 s XPS spectra of Ni-SAC-2. (f) Normalized Ni K-edge XANES spectra, and (g) Fourier transform of the EXAFS spectra of Ni foil, NiO, NiPc and Ni-SAC-2.

from 1.0 wt% to 4.0 wt%. These were designated as Ni-SAC-1 (1.0 wt %), Ni-SAC-2 (3.0 wt%), and Ni-SAC-3 (3.7 wt%), respectively (Table S2, Figs. S3–S14).

Scanning electron microscopy (SEM) analysis of the three Ni-SAC catalysts (Fig. 2b and Fig. S3) revealed well-dispersed granular morphologies with an average particle size of approximately 500 nm. These particles are randomly assembled into a three-dimensional porous carbon framework, as further confirmed by transmission electron microscopy (TEM) (Fig. S4). High-resolution scanning transmission electron microscopy (STEM) analysis verified the predominant presence of single metal sites on the surfaces of all three samples (Fig. 2c and Fig. S5). Taking Ni-SAC-2 as an example, energy-dispersive X-ray spectroscopy (EDX) elemental mapping showed a uniform distribution of Ni, N, and C elements on the polyhedral carbon supports (Fig. 2d). X-ray photoelectron spectroscopy (XPS) analysis further confirmed the presence of Ni–N bonds (Fig. 2e), where the oxidation state of Ni is between 0 and + 2 (Fig. S6) [46–48]. This is consistent with the Ni K-edge X-ray absorption near-edge structure (XANES) analysis (Fig. 2f). The Fourier-transform of the extended X-ray absorption fine structure (EXAFS) spectra (Fig. 2g), along with the corresponding fitting results (Figs. S7–S8 and Table S3), revealed predominant Ni−N/O coordination, with a characteristic peak at 1.38 Å observed for Ni-SAC-2. A secondary peak at 2.08 Å corresponds to the Ni–Ni path, indicating the presence of Ni or NiO clusters on the carbon surface [49–51]. For Ni-SAC-3, Ni nanoparticles were detected (Fig. S9 and Fig. S11). These results suggest that, with increasing amounts of the Ni sublimation source during the CVD process, a portion of Ni atoms aggregated into Ni clusters in Ni-SAC-2 and further into Ni nanoparticles in Ni-SAC-3.

We further conducted linear combination fitting (LCF) of the XANES spectra to determine the distribution of Ni species in the three samples (Fig. S10 and Table S4). The results indicate that Ni-SAC-1 consists exclusively of Ni single atoms; Ni-SAC-2 comprises 76 % Ni single atoms, 18 % NiO, and 6 % metallic Ni; and Ni-SAC-3 contains 69 % Ni single atoms, 17 % NiO, and 14 % metallic Ni. The absolute contents of these species were quantified by correlating the LCF results with inductively coupled plasma atomic emission spectrometry (ICP-AES) measurements (Table S2). Specifically, Ni-SAC-1 contains 1.0 wt% Ni single atoms, whereas Ni-SAC-2 contains 2.3 wt% Ni single atoms and 0.7 wt% Ni/NiO species, which are ascribed to Ni/NiO clusters due to the absence of distinct Ni metal reflections in the XRD pattern (Fig. S10).

Ni-SAC-3 possesses a comparable Ni single-atom content (2.6 wt%) to Ni-SAC-2; however, it exhibits a higher loading of NiO/Ni species (1.1 wt%), which are present in the form of Ni nanoparticles (Fig. S11). It has been reported that Ni clusters can synergistically promote the electrocatalytic activity of Ni single atoms toward CO_2-to-CO conversion, whereas Ni nanoparticles predominantly facilitate the competing HER during CO_2 electrolysis [52–55]. This compositional distinction highlights Ni-SAC-2 as a particularly promising catalyst for enhancing CO_2-to-CO conversion rates in reactive capture systems.

3.2. Ni-SAC catalyst for CO electrosynthesis in a reactive capture system

We evaluated the catalytic performance of the three Ni-SAC catalysts in a membrane electrode assembly (MEA) electrolyser-based reactive capture system [21]. Carbon dioxide was purged into 2 M KOH solution to simulate the capture process, and the capture solution (pH ~9.6) was fed to the electrolyser for electrochemical CO_2 conversion (Fig. 1, Fig. S15-S18). The CO_2 regeneration arises from the reaction between the CO_2-loaded alkaline solution and protons electromigrated from the anode, in agreement with previous reports (Fig. S16) [20,21]. The pH of the capture solution remained nearly unchanged during 10 min electrolysis at 100 mA cm^{-2}, indicating minimal CO_2 consumption (Fig. S17). VLE modeling confirmed that the observed buffering capacity suffices to sustain CO_2 regeneration, and the CO_2 loading capacity of 2 M KOH at pH ~9.6 was estimated to be ~0.87 mol CO_2 per mol KOH, consistent with reported values (Fig. S18) [56]. Only H_2 and CO were detected at the cathode outlet. All three catalysts exhibited similar trends in CO production across the current density range of 50–300 mA cm^{-2}, with CO Faradaic efficiencies (FEs) peaking around 100 mA cm^{-2} (Fig. 3a). Among them, Ni-SAC-2 – with its higher loading of Ni single atoms – achieved significantly greater CO FEs and better HER suppression compared to Ni-SAC-1. Notably, further increasing the Ni loading, as in Ni-SAC-3, did not result in a proportional enhancement in CO production. Ni-SAC-2 contains 2.3 wt% Ni single atoms and 0.7 wt % NiO/Ni clusters, while Ni-SAC-3 has 2.6 wt% Ni single atoms accompanied by 1.1 wt% NiO/Ni nanoparticles. Although small NiO/Ni clusters can contribute positively to CO_2-to-CO conversion, larger NiO/Ni nanoparticles tend to promote hydrogen evolution instead [52–55]. Typically, at 100 mA cm^{-2}, a peak CO FE of 68 % with a CO/H_2 ratio of ~2.0 was achieved for Ni-SAC-2, 1.4 times larger than that of Ni-SAC-1 (48 %) and Ni-SAC-3 (47 %) (Fig. 3a, Figs. S19-S21). At a higher current density of 200 mA cm^{-2}, Ni-SAC-2 maintained a relatively high CO FE of 61 % and a CO_2 conversion rate of 89 %, much higher than those reported in prior reactive capture systems (Table S1). Notable, the maximum TOF of Ni-SAC-1 reaches 11142.2 h^{-1} at 200 mA cm^{-2}, which exceeds the performance of previously reported reactive capture systems employing Ni-based single-atom catalysts (Fig. S22). The Ni-SAC-2 catalyst also exhibited larger CO production rate, i.e., CO partial current density (j_{CO}), compared with the other two catalysts. At 300 mA cm^{-2}, its j_{CO} reached 140 mA cm^{-2} with a full-cell voltage of 5.1 V (Fig. 3b). The Ni-SAC-2 electrode exhibited excellent stability for CO production. The CO FE kept more than 50 % during 100 h electrolysis at 100 mA cm^{-2}, with a CO/H_2 ratio of ~ 1.0, a minimal full-cell voltage drop of ~5 mV h^{-1} and capture solution pH were stable (Fig. 3c and Fig. S23). The electrode microstructure and Ni-N coordination were nearly unchanged after the prolonged electrolysis, verifying the robustness of Ni-SAC-2 (Figs. S24–S25). N *1 s* XPS analysis of the spent catalyst further confirmed the structural integrity of

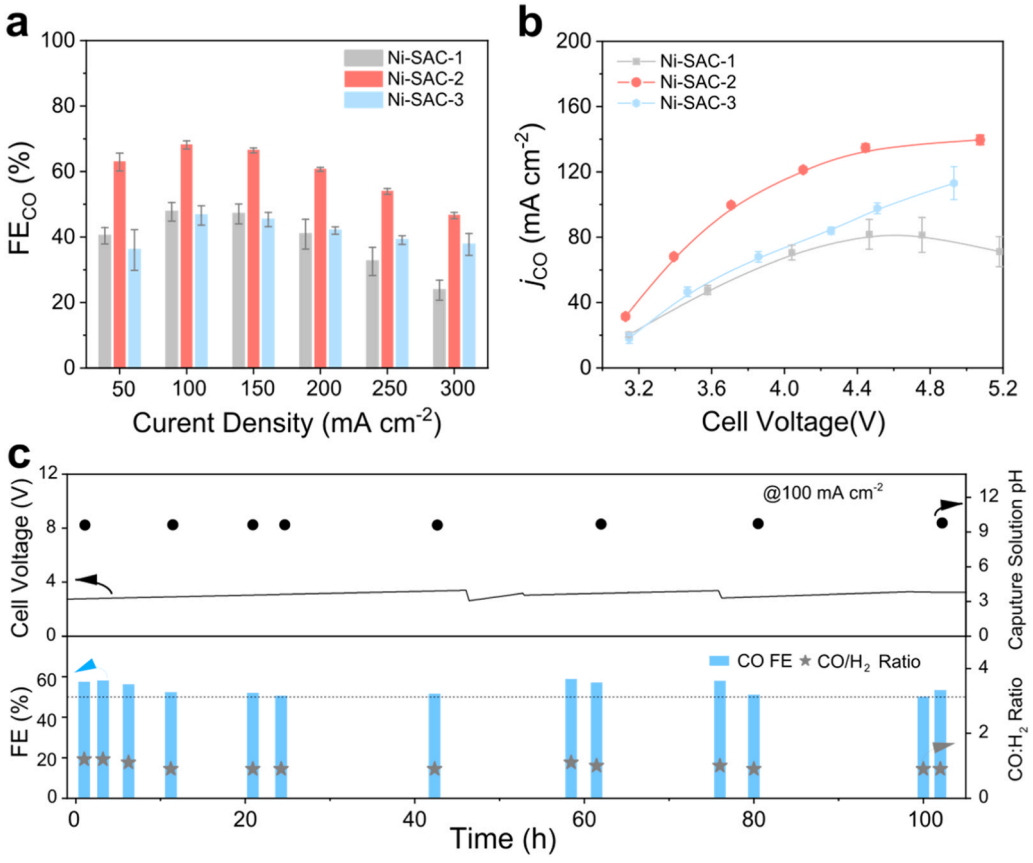

Fig. 3. Electrocatalytic performance of Ni-SAC catalysts for KOH-based reactive capture. (a) CO FE as a function of applied current densities for Ni-SAC catalysts with different Ni loading. (b) CO partial current densities for Ni-SAC electrodes at different applied potentials. (c) Long-term operation of Ni-SAC-2 catalyst for reactive capture over 100 h at 100 mA cm^{-2}, with the variation of CO FE, CO/H_2 ratio, cell voltage (initial voltage: 2.8 V), and the capture solution pH. Error bars represent standard deviations of three independent measurements.

Ni-N_4 sites (Fig. S25), with the Ni-N coordination fraction decreasing only slightly from 23.9 % before electrolysis (Figs. 2e) to 22.0 % after 100 h of continuous operation. This negligible variation highlights the exceptional stability of the atomically dispersed Ni sites under extended electrochemical conditions. Furthermore, high-resolution TEM images and XRD patterns revealed no observable aggregation of Ni/NiO nanoparticles under the same conditions (Fig. S26). These results collectively exclude the possibility of structural reconstruction of Ni-SAC-2 during long-term electrolysis [57–59].

3.3. The impacts of Ni-SAC catalyst microenvironment on CO electrosynthesis

Despite the promotional effect of high-density active sites, the microenvironment within the Ni-SAC catalyst layer – such as local pH and ion/gas transport – plays a critical role in regulating CO_2 regeneration and the accessibility of in situ generated CO_2 to the Ni catalytic sites [60–63]. To decouple these effects, we conducted a systematic investigation using the Ni-SAC-2 catalyst.

The regeneration of CO_2 in the reactive capture system arises from the reaction between the capture solution and protons electromigrated from the anode. The proton flux towards the cathode influences the availability of CO_2 reactant (Fig. 1). To investigate this effect, we varied the proton concentration in the anolyte. Increasing the proton concentration from 0.05 M to 0.1 M resulted in a significant enhancement in electrocatalytic CO production (Fig. 4a, and Fig. S27). At 100 mA cm^{-2}, the 0.1 M anolyte achieved a CO FE of 68 %, which is1.2 times larger than that obtained with the 0.05 M anolyte (FE_{CO} ~ 59 %). Ion permeation tests confirmed that the 0.1 M anolyte generated a higher proton flux across the CEM – 1.035 μmol s^{-1} cm^{-2} compared to 1.026 μmol s^{-1} cm^{-2} with the 0.05 M solution (Fig. 4b, and Fig. S28). This increased proton flux enhanced CO_2 production at the catalyst/CEM interface (Fig. 1b), as evidenced by the elevated CO_2 concentration measured at the cathode outlet (Fig. 4b). Further increase in proton concentration did not significantly improve the proton flux, CO_2 regeneration, or CO production.

We further investigated the impacts of catalyst microenvironment on the transport of *in situ* regenerated CO_2 to the active sites. By varying the Ni-SAC-2 catalyst layer thickness from 2 μm to 8 μm (Fig. 4c, Fig. S29 and Fig. S30), we identified an optimal CO production performance with a 6 μm-thick catalyst layer. This electrode showed significantly higher CO FE and CO production rates than the 2 μm and 8 μm counterparts. At a current density of 200 mA cm^{-2}, the 6 μm electrode achieved a CO FE of 61 % and a j_{CO} of 121 mA cm^{-2}, 1.4 times and 1.9 times larger than those of 8 μm (45 %, 89 mA cm^{-2}) and 2 μm (32 %, 64 mA cm^{-2}) electrodes, respectively. CO_2 flux measurements revealed that the 6 μm catalyst layer delivered a higher CO_2 flux across the electrode (0.807 μmol s^{-1} cm^{-2}) compared to the 2 μm layer (0.411 μmol s^{-1} cm^{-2}) (Fig. S31). This trend was further supported by one-dimensional diffusion-reaction model simulation (Fig. S32). Increasing the catalyst layer thickness beyond 6 μm did not lead to further improvement in CO_2 flux or CO production.

In addition to catalyst layer thickness, ionomers dispersed among catalyst particles play a key role in facilitating CO_2 transport to active sites during CO_2R. To investigate the impacts of ionomers in the reactive capture system, we employed the widely used perfluorosulfonic acid (PFSA) ionomer, which contains both hydrophobic and hydrophilic domains, and fabricated 6 μm catalyst layers with varying PFSA contents (7 wt%, 13 wt%, and 37 wt%) (Fig. 4d, Figs. S33-S34). The catalyst layer containing 13 wt% PFSA delivered superior performance compared to those with 7 wt% case and 37 wt% case, in terms of CO FE and j_{CO}. This highlights the importance of optimizing the hydrophobic/hydrophilic balance within the catalyst layer to effectively manage the local ion/gas microenvironment and promote conversion of in situ

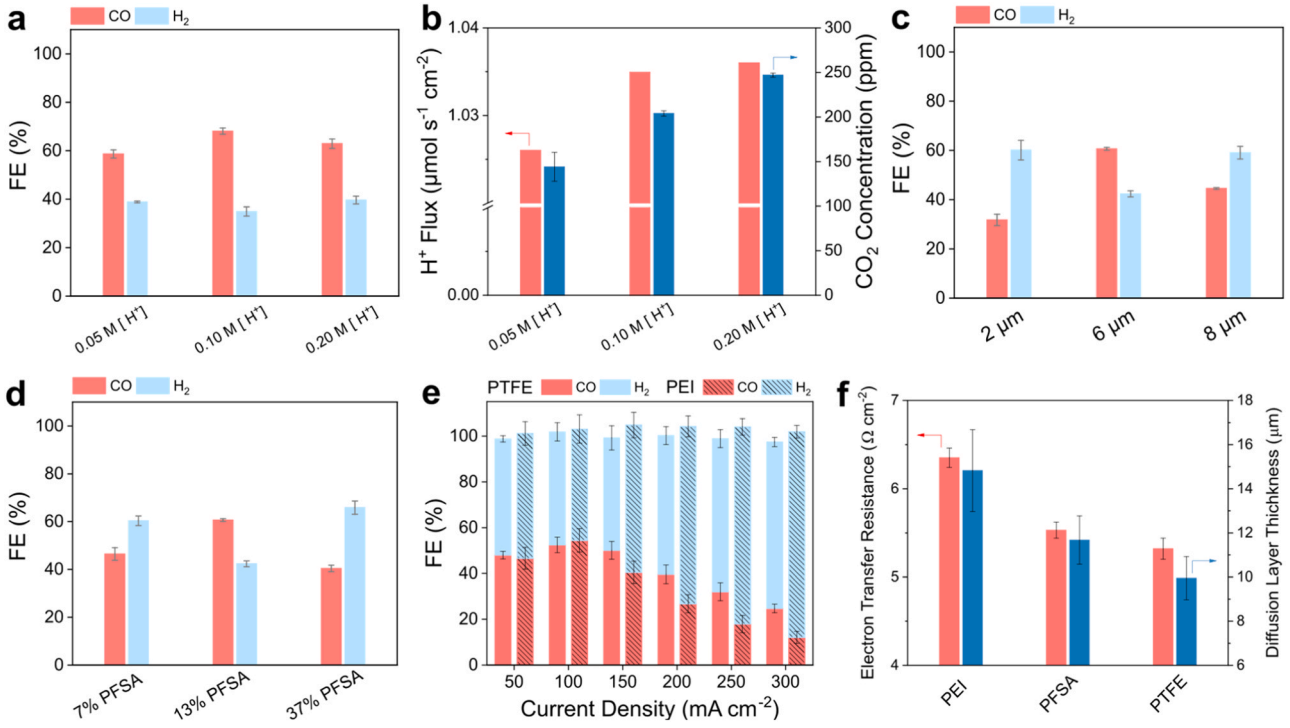

Fig. 4. Decoupling the impacts of Ni-SAC catalyst microenvironment on CO electrosynthesis in reactive capture. (a) The electrocatalytic performance of Ni-SAC-2 catalyst using H_2SO_4 anolyte with various proton concentration at 100 mA cm^{-2}. (b) The apparent proton flux and CO_2 concentration at the cathode outlet measured at 100 mA cm^{-2} for three different anolytes. (c) Impact of Ni-SAC-2 catalyst layer thickness on electrocatalytic performance at 200 mA cm^{-2}. (d) Impact of PFSA ionomer content in 6 μm-thick Ni-SAC-2 catalyst layer on electrocatalytic performance at 200 mA cm^{-2}. (e) Impact of PTFE and PEI ionomer in the Ni-SAC-2 catalyst layers on electrocatalytic performance at current densities from 50 to 300 mA cm^{-2}. (f) Electron transfer resistance and CO_2 diffusion layer thicknesses measured or calculated for the 6 μm-thick catalysts layers with three different additives including PEI, PFSA, and PTFE.

regenerated CO_2 [64]. This was further supported by controls using highly hydrophilic polyethyleneimine (PEI) and hydrophobic polytetrafluoroethylene (PTFE) as alternative additives (Fig. 4e, Figs. S35-S37). Notably, the Ni-SAC-2 electrode with 13 wt% PFSA exhibited a CO FE of 61 % and a j_{CO} of 121 mA cm^{-2} at 200 mA cm^{-2}, 2.3 times and 1.5 times higher than those obtained with PEI (27 %, 54 mA cm^{-2}) and PTFE (40 %, 79 mA cm^{-2}), respectively. Electrochemical impedance spectroscopy (EIS) analysis revealed that the hydrophilic domains within the ionomers facilitate charge transfer at the catalyst/electrolyte interface, while hydrophobic domains enhance CO_2 mass transport (Fig. 4f, Fig. S38 and Table S8, see *EIS section* for more details).

The above results highlight the crucial role of the Ni-SAC catalyst microenvironment in governing CO_2 regeneration and transport for efficient CO electrosynthesis in the reactive capture system. Optimizing both the catalyst layer thickness and interfacial proton flux enhances the local CO_2 regeneration at the catalyst/CEM interface, ensuring a sufficient supply of reactants for electrochemical conversion. Meanwhile, improving CO_2 transport within the catalyst layer, modulated by ionomer content and hydrophobicity, reduces mass transfer resistance and facilitates effective delivery of CO_2 to the active sites. Together, these two mechanisms work synergistically to enhance CO_2-to-CO conversion efficiency and boost CO production rates in the reactive capture system.

3.4. Energy consumption analysis

Our reactive capture system, integrated with a high-density Ni-SAC catalyst and an optimized catalyst microenvironment, achieved an energy consumption of 37.7 GJ ton_{CO}^{-1} for CO electrosynthesis. This represents a 30 % and 50 % increase in energy efficiency compared to previously reported amine-based reactive capture system (62.2 GJ ton_{CO}^{-1}) and KOH-based reactive capture systems (56.9 GJ ton_{CO}^{-1}) (Fig. 5 and Table S9), respectively. Despite these improvements, it is important to note that the energy consumption associated with the CO_2 electrolysis component in our system (34.2 GJ ton_{CO}^{-1}) remains higher than that of pure-CO_2 electrolysis system (23.0 GJ ton_{CO}^{-1}). These results highlight the substantial progress made, while also underscoring the need for further innovation in catalyst design and microenvironment engineering to improve the overall energy efficiency of reactive capture systems.

4. Conclusions

We developed a nickel single-atom catalyst (Ni-SAC) featuring a high density of active Ni sites (>1.0 wt% Ni loading) and a systematically engineered microenvironment to enable efficient CO electrosynthesis in a hydroxide-mediated reactive capture system. By concurrently optimizing the catalyst structure and its local reaction environment, we achieved a CO Faradaic efficiency of 61 % and a CO_2 conversion rate of 89 % at a current density of 200 mA cm^{-2}, with stable operation maintained for over 100 h. These performance metrics surpass those of previously reported reactive capture systems. Combined experimental and computational analyses reveal that, beyond catalyst design, CO_2 regeneration and mass transport to active sites are critical factors governing CO production in such systems. This study underscores the dual importance of catalyst architecture and microenvironmental control, offering practical strategies to advance the electrocatalytic performance of next-generation reactive capture technologies.

CRediT authorship contribution statement

Cheng Wang: Writing – original draft, Visualization, Methodology, Investigation, Formal analysis, Data curation. **Manman Qi:** Methodology, Investigation. **Zhi Zheng:** Validation, Investigation. **Xiaobo Zheng:** Visualization, Methodology, Investigation. **Shuai Li:** Visualization, Methodology, Investigation. **Peng Li:** Methodology, Investigation. **Tianyi Ma:** Resources, Investigation. **Bernt Johannessen:** Methodology, Investigation. **Yitong Cao:** Investigation. **Jiaobao Yi:** Resources, Investigation. **Hai Yu:** Writing – review & editing, Supervision, Resources, Project administration, Methodology, Investigation, Funding acquisition. **Jie Zeng:** Writing – review & editing, Supervision, Resources, Project administration, Funding acquisition. **Yong Zhao:** Writing – review & editing, Supervision, Project administration, Methodology, Funding acquisition, Formal analysis, Conceptualization.

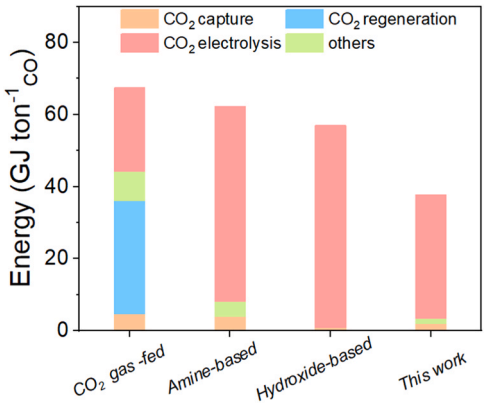

Fig. 5. Energy consumption analysis. Comparison of energy cost associated with CO production in gas-phase CO_2 electrolysis, amine- based reactive capture, and hydroxide-based reactive capture systems.

Declaration of Competing Interest

The authors declare that they have no known competing financial interests or personal relationships that could have appeared to influence the work reported in this paper.

Acknowledgments

This work was supported by the National Key Research and Development Program of China (2021YFA1500500), CAS Project for Young Scientists in Basic Research (YSBR-051), NSFC (22525021, 22221003, 22250007, 22361162655), the Science and Technology Development Fund (FDCT) of Macao S.A.R (0070/2023/AFJ), Fundamental Research Funds for the Central Universities, the Joint Fund of the Yulin University and the Dalian National Laboratory for Clean Energy (YLU-DNL Fund 2022012), the State Key Laboratory of Catalysis (2024SKL-A-011), and International Partnership Program of Chinese Academy of Sciences (123GJHZ2022101GC) for financial supports. J.Z. also acknowledges support from the New Cornerstone Science Foundation through the XPLORER PRIZE. H. Y., Y. Z. and Z. Z. acknowledge support from the CSIRO-CAS partnership fund. Y. Z. acknowledge the grant for XAS beamtime (M21384) at the Australian Synchrotron, part of ANSTO, and the Australian Research Council Discovery Early Career Researcher Award (DE250101462) funded by the Australian Government. C. W. acknowledge the China Scholarship Council for scholarship support. C. W. also acknowledge Shuzhen Zhang, Dongfang Li and Yuwei Wang for their assistance in materials characterization.

Appendix A. Supporting information

Supplementary data associated with this article can be found in the online version at doi:10.1016/j.apcatb.2025.126068.

Data availability

Data will be made available on request.

References

[1] X. Zhang, Y. Wang, M. Gu, M. Wang, Z. Zhang, W. Pan, Z. Jiang, H. Zheng, M. Lucero, H. Wang, G.E. Sterbinsky, Q. Ma, Y.G. Wang, Z. Feng, J. Li, H. Dai, Y. Liang, Molecular engineering of dispersed nickel phthalocyanines on carbon nanotubes for selective CO_2 reduction, Nat. Energy 5 (2020) 684–692.

[2] M.C.O. Monteiro, M.F. Philips, K.J.P. Schouten, M.T.M. Koper, Efficiency and selectivity of CO_2 reduction to CO on gold gas diffusion electrodes in acidic media, Nat. Commun. 12 (2021) 4943.

[3] J. Li, H. Zeng, X. Dong, Y. Ding, S. Hu, R. Zhang, Y. Dai, P. Cui, Z. Xiao, D. Zhao, L. Zhou, T. Zheng, J. Xiao, J. Zeng, C. Xia, Selective CO_2 electrolysis to CO using isolated antimony alloyed copper, Nat. Commun. 14 (2023) 340.

[4] X. Song, Z. Guo, A new process for synthesis gas by co-gasifying coal and natural gas, Fuel 84 (2005) 525–531.

[5] Y. Cao, Z. Gao, J. Jin, H. Zhou, M. Cohron, H. Zhao, H. Liu, W. Pan, Synthesis gas production with an adjustable H_2/CO ratio through the coal gasification process: effects of coal ranks and methane addition, Energy Fuels 22 (2008) 1720–1730.

[6] P. Gangadharan, A. Zanwar, K. Zheng, J. Gossage, H.H. Lou, Sustainability assessment of polygeneration processes based on syngas derived from coal and natural gas, Comput. Chem. Eng. 39 (2012) 105–117.

[7] J. Ling, H. Yang, G. Tian, J. Cheng, X. Wang, X. Yu, Direct reduction of iron to facilitate net zero emissions in the steel industry: a review of research progress at different scales, J. Clean. Prod. 441 (2024) 140933.

[8] H. Liu, Y. Tang, X. Ma, J. Tang, W. Yue, Biomass gasification based on sorption-enhanced hydrogen production coupled with carbon utilization to produce tunable syngas for methanol synthesis, Energy Convers. Magn. 309 (2024) 118428.

[9] D.W. Keith, G. Holmes, D. St. Angelo, K. Heidel, A process for capturing CO_2 from the atmosphere, Joule 2 (2018) 1573–1594.

[10] M. Fasihi, O. Efimova, C. Breyer, Techno-economic assessment of CO_2 direct air capture plants, J. Clean. Prod. 224 (2019) 957–980.

[11] E.W. Lees, B.A.W. Mowbray, F.G.L. Parlane, C.P. Berlinguette, Gas diffusion electrodes and membranes for CO_2 reduction electrolysers, Nat. Rev. Mater. 7 (2022) 55–64.

[12] S. Zhang, C. Chen, K. Li, H. Yu, F. Li, Materials and system design for direct electrochemical CO_2 conversion in capture media, J. Mater. Chem. A. 9 (2021) 18785–18792.

[13] M. Li, K. Yang, M. Abdinejad, C. Zhao, T. Burdyny, Advancing integrated CO_2 electrochemical conversion with amine-based CO_2 capture: a review, Nanoscale 14 (2022) 11892–11908.

[14] M. Li, E. Irtem, H.P. Iglesias van Montfort, M. Abdinejad, T. Burdyny, Energy comparison of sequential and integrated CO_2 capture and electrochemical conversion, Nat. Commun. 13 (2022) 5398.

[15] Y.C. Li, G. Lee, T. Yuan, Y. Wang, D.H. Nam, Z. Wang, F.P. García de Arquer, Y. Lum, C.-T. Dinh, O. Voznyy, E.H. Sargent, CO_2 electroreduction from carbonate electrolyte, ACS Energy Lett. 4 (2019) 1427–1431.

[16] G. Lee, Y.C. Li, J.Y. Kim, T. Peng, D.H. Nam, A. Sedighian Rasouli, F. Li, M. Luo, A. H. Ip, Y.C. Joo, E.H. Sargent, Electrochemical upgrade of CO_2 from amine capture solution, Nat. Energy 6 (2021) 46–53.

[17] J.H. Kim, H. Jang, G. Bak, W. Choi, H. Yun, E. Lee, D. Kim, J. Kim, S.Y. Lee, Y. J. Hwang, The insensitive cation effect on a single atom ni catalyst allows selective electrochemical conversion of captured CO_2 in universal media, Energy Environ. Sci. 15 (2022) 4301–4312.

[18] K.M.G. Langie, K. Tak, C. Kim, H.W. Lee, K. Park, D. Kim, W. Jung, C.W. Lee, H.-S. Oh, D.K. Lee, J.H. Koh, B.K. Min, D.H. Won, U. Lee, Toward economical application of carbon capture and utilization technology with near-zero carbon emission, Nat. Commun. 13 (2022) 7482.

[19] H. Li, J. Gao, J. Shan, Q. Du, Y. Zhang, X. Guo, S. Wu, Z. Wang, Boosting the direct conversion of NH_4HCO_3 electrolyte to syngas on Ag/Zn zeolitic imidazolate framework derived nitrogen-carbon skeleton, Front. Chem. Sci. Eng. 17 (2023) 1196–1207.

[20] G. Lee, A.S. Rasouli, B.H. Lee, J. Zhang, D.H. Won, Y.C. Xiao, J.P. Edwards, M. G. Lee, E.D. Jung, F. Arabyarmohammadi, H. Liu, I. Grigioni, J. Abed, T. Alkayyali, S. Liu, K. Xie, R.K. Miao, S. Park, R. Dorakhan, Y. Zhao, C.P. O'Brien, Z. Chen, D. Sinton, E. Sargent, CO_2 electroreduction to multicarbon products from carbonate capture liquid, Joule 7 (2023) 1277–1288.

[21] Y.C. Xiao, C.M. Gabardo, S. Liu, G. Lee, Y. Zhao, C.P. O'Brien, R.K. Miao, Y. Xu, J. P. Edwards, M. Fan, J.E. Huang, J. Li, P. Papangelakis, T. Alkayyali, A. Sedighian Rasouli, J. Zhang, E.H. Sargent, D. Sinton, Direct carbonate electrolysis into pure syngas, EES Catal. 1 (2023) 54–61.

[22] J.I. Huertas, M.D. Gomez, N. Giraldo, J. Garzón, CO_2 absorbing capacity of MEA, J. Chem. 2015 (2015) 1–7.

[23] N. McCann, D. Phan, X. Wang, W. Conway, R. Burns, M. Attalla, G. Puxty, M. Maeder, Kinetics and mechanism of carbamate formation from CO_2 (aq), carbonate species, and monoethanolamine in aqueous solution, J. Phys. Chem. A. 113 (2009) 5022–5029.

[24] I. Sullivan, A. Goryachev, I.A. Digdaya, X. Li, H.A. Atwater, D.A. Vermaas, C. Xiang, Coupling electrochemical CO_2 conversion with CO_2 capture, Nat. Catal. 4 (2021) 952–958.

[25] H. Ma, E. Ibáñez-Alé, R. Ganganahalli, J. Pérez-Ramírez, N. López, B.S. Yeo, Direct electroreduction of carbonate to formate, J. Am. Chem. Soc. 145 (2023) 24707–24716.

[26] S.C. Maberly, B. Gontero, Ecological imperatives for aquatic CO_2-concentrating mechanisms, J. Exp. Bot. 68 (2017) 3797–3814.

[27] M. König, J. Vaes, E. Klemm, D. Pant, Solvents and supporting electrolytes in the electrocatalytic reduction of CO_2, iScience 19 (2019) 135–160.

[28] D. Raciti, M. Mao, C. Wang, Mass transport modelling for the electroreduction of CO_2 on cu nanowires, Nanotechnology 29 (2018) 44001.

[29] Z. Xing, L. Hu, D.S. Ripatti, X. Hu, X. Feng, Enhancing carbon dioxide gas-diffusion electrolysis by creating a hydrophobic catalyst microenvironment, Nat. Commun. 12 (2021) 136.

[30] N.B. Watkins, Z.J. Schiffer, Y. Lai, C.B. Musgrave, H.A. Atwater, W.A. Goddard, T. Agapie, J.C. Peters, J.M. Gregoire, Hydrodynamics change tafel slopes in electrochemical CO_2 reduction on copper, ACS Energy Lett. 8 (2023) 2185–2192.

[31] D. Xu, K. Li, B. Jia, W. Sun, W. Zhang, X. Liu, T. Ma, Electrocatalytic CO_2 reduction towards industrial applications, Carbon Energy 5 (2023) e230.

[32] V.G. Agarwal, S. Haussener, Quantifying mass transport limitations in a microfluidic CO_2 electrolyzer with a gas diffusion cathode, Commun. Chem. 7 (2024) 47.

[33] G. Leverick, E.M. Bernhardt, A.I. Ismail, J.H. Law, A. Arifutzzaman, M.K. Aroua, B. M. Gallant, Uncovering the active species in amine-mediated CO_2 reduction to CO on ag, ACS Catal. 13 (2023) 12322–12337.

[34] M. Wen, N. Sun, L. Jiao, S. Zang, H. Jiang, Microwave-assisted rapid synthesis of MOF-based single-atom ni catalyst for CO_2 electroreduction at ampere-level current, Angew. Chem. Int. Ed. 63 (2024) e202318338.

[35] Y. Wang, J. Kim, H.D. Jung, J. Liu, K. Ye, C. Xia, S. Back, K. Jiang, Understanding the first activation step of electrochemical CO_2 reduction over ag and Ni-N-C active sites, Nano Energy 127 (2024) 109728.

[36] C. Wang, H. Ren, Z. Wang, Q. Guan, Y. Liu, W. Li, A promising single-atom Co-N-C catalyst for efficient CO_2 electroreduction and high-current solar conversion of CO_2 to CO, Appl. Catal. B Environ. 304 (2022) 120958.

[37] F. Yang, P. Song, X. Liu, B. Mei, W. Xing, Z. Jiang, L. Gu, W. Xu, Highly efficient CO_2 electroreduction on ZnN_4 -based single-atom catalyst, Angew. Chem. Int. Ed. 57 (2018) 12303–12307.

[38] X. Li, S. Xi, L. Sun, S. Dou, Z. Huang, T. Su, X. Wang, Isolated FeN_4 sites for efficient electrocatalytic CO_2 reduction, Adv. Sci. 7 (2020) 2001545.

[39] L. Jiao, W. Yang, G. Wan, R. Zhang, X. Zheng, H. Zhou, S. Yu, H. Jiang, Single-atom electrocatalysts from multivariate metal-organic frameworks for highly selective reduction of CO_2 at low pressures, Angew. Chem. Int. Ed. 59 (2020) 20589–20595.

[40] W. Ren, X. Tan, W. Yang, C. Jia, S. Xu, K. Wang, S.C. Smith, C. Zhao, Isolated diatomic Ni-Fe metal–nitrogen sites for synergistic electroreduction of CO_2, Angew. Chem. Int. Ed. 58 (2019) 6972–6976.

[41] D. Kim, C. Xie, N. Becknell, Y. Yu, M. Karamad, K. Chan, E.J. Crumlin, J. K. Nørskov, P. Yang, Electrochemical activation of CO_2 through atomic ordering transformations of AuCu nanoparticles, J. Am. Chem. Soc. 139 (2017) 8329–8336.

[42] Y. Wu, C. Chen, X. Yan, X. Sun, Q. Zhu, P. Li, Y. Li, S. Liu, J. Ma, Y. Huang, B. Han, Boosting CO_2 electroreduction over a cadmium single-atom catalyst by tuning of the axial coordination structure, Angew. Chem. Int. Ed. 60 (2021) 20803–20810.

[43] D. Yao, C. Tang, X. Zhi, B. Johannessen, A. Slattery, S. Chern, S. Qiao, Inter-metal interaction with a threshold effect in NiCu dual-atom catalysts for CO_2 electroreduction, Adv. Mater. 35 (2023) 2209386.

[44] Y.C. Xiao, S.S. Sun, Y. Zhao, R.K. Miao, M. Fan, G. Lee, Y. Chen, C.M. Gabardo, Y. Yu, C. Qiu, Z. Guo, X. Wang, P. Papangelakis, J.E. Huang, F. Li, C.P. O'Brien, J. Kim, K. Han, P.J. Corbett, J.Y. Howe, E.H. Sargent, D. Sinton, Reactive capture of CO_2 via amino acid, Nat. Commun. 15 (2024) 7849.

[45] M. Qi, M.J. Zachman, Y. Li, Y. Zeng, S. Hwang, J. Liang, M. Lyons, Q. Zhao, Y. Mao, Y. Shao, Z. Feng, Z. Wang, Y. Zhao, G. Wu, Highly dense atomic Fe–Ni dual metal sites for efficient CO_2 to CO electrolyzers at industrial current densities, Energy Environ. Sci. 18 (2025) 5643–5656.

[46] X. Wang, X. Sang, C. Dong, S. Yao, L. Shuai, J. Lu, B. Yang, Z. Li, L. Lei, M. Qiu, L. Dai, Y. Hou, Proton capture strategy for enhancing electrochemical CO_2 reduction on atomically dispersed metal–nitrogen active sites, Angew. Chem. Int. Ed. 60 (2021) 11959–11965.

[47] Z. Zeng, L.Y. Gan, H. Bin Yang, X. Su, J. Gao, W. Liu, H. Matsumoto, J. Gong, J. Zhang, W. Cai, Z. Zhang, Y. Yan, B. Liu, P. Chen, Orbital coupling of hetero-diatomic nickel-iron site for bifunctional electrocatalysis of CO_2 reduction and oxygen evolution, Nat. Commun. 12 (2021) 4088.

[48] H. Song, C.A. Fernández, H. Choi, P.-W. Huang, J. Oh, M.C. Hatzell, Integrated carbon capture and CO production from bicarbonates through bipolar membrane electrolysis, Energy Environ. Sci. 17 (2024) 3570–3579.

[49] C. Zhao, X. Dai, T. Yao, W. Chen, X. Wang, J. Wang, J. Yang, S. Wei, Y. Wu, Y. Li, Ionic exchange of metal–organic frameworks to access single nickel sites for efficient electroreduction of CO_2, J. Am. Chem. Soc. 139 (2017) 8078–8081.

[50] S. Wang, Z. Qian, Q. Huang, Y. Tan, F. Lv, L. Zeng, C. Shang, K. Wang, G. Wang, Y. Mao, Y. Wang, Q. Zhang, L. Gu, S. Guo, Industrial-level CO_2 electroreduction using solid-electrolyte devices enabled by high-loading nickel atomic site catalysts, Adv. Energy Mater. 12 (2022) 2201278.

[51] L. Han, H. Cheng, W. Liu, H. Li, P. Ou, R. Lin, H.T. Wang, C.W. Pao, A.R. Head, C.-H. Wang, X. Tong, C.J. Sun, W.F. Pong, J. Luo, J.C. Zheng, H.L. Xin, A single-atom library for guided monometallic and concentration-complex multimetallic designs, Nat. Mater. 21 (2022) 681–688.

[52] H. Li, K. Gan, R. Li, H. Huang, J. Niu, Z. Chen, J. Zhou, Y. Yu, J. Qiu, X. He, Highly dispersed NiO clusters induced electron delocalization of Ni-N-C catalysts for enhanced CO_2 electroreduction, Adv. Funct. Mater. 33 (2023) 2208622.

[53] R. Zhao, Y. Wang, G. Ji, J. Zhong, F. Zhang, M. Chen, S. Tong, P. Wang, Z. Wu, B. Han, Z. Liu, Partially nitrided ni nanoclusters achieve energy-efficient electrocatalytic CO_2 reduction to CO at ultralow overpotential, Adv. Mater. 35 (2023) 2205262.

[54] Y. Song, J. Mao, C. Zhu, S. Li, G. Li, X. Dong, Z. Jiang, W. Chen, W. Wei, Ni nanoclusters anchored on Ni-N-C sites for CO_2 electroreduction at high current densities, ACS Appl. Mater. Interfaces 15 (2023) 10785–10794.

[55] Q. Pan, Y. Chen, H. Li, G. Ma, S. Jiang, X. Cui, L. Zhang, Y. Bao, T. Ma, Size effect of nickel from nanoparticles to clusters to single atoms for electrochemical CO_2 reduction, J. Mater. Chem. A. 12 (2024) 20035–20044.
[56] N. Firman, A. Noor, M. Zakir, M. Maming, A. Fathurrahman, A. Fathurrahman, Absorption of carbon dioxide into potassium hydroxide: preliminary study for its application into liquid scintillation counting procedure, Egypt, J. Chem. 64 (2021) 4907–4912.
[57] A. Huang, T. Zhou, J. Zhang, Y. Zhang, Y. Wu, Y. Wang, W. Luo, Competing CO and HCOOH pathways in CO_2 electroreduction, ChemCatChem 16 (2024) e202400504.
[58] C.D. Koolen, J.K. Pedersen, B. Zijlstra, M. Winzely, J. Zhang, T.V. Pfeiffer, W. Vrijburg, M. Li, A. Agarwal, Z. Akbari, Y. Kuddusi, J. Herranz, O.V. Safonova, A. Schmidt-Ott, W. Luo, A. Zuettel, Scalable synthesis of Cu-cluster catalysts via spark ablation for the electrochemical conversion of CO_2 to acetaldehyde, Nat. Synth. 4 (2025) 336–346.
[59] Z. Wang, F. Zhou, B. Lv, J. Yu, J. Zhang, Y. Zhang, Y. Wu, Y. Wang, W. Luo, Unveiling pH-dependent mechanistic shifts in Cu_2O-catalyzed nitrate electroreduction for selective ammonia synthesis, Adv. Sustain. Syst. (2025) e00211.
[60] J. Li, Z. Wang, C. McCallum, Y. Xu, F. Li, Y. Wang, C.M. Gabardo, C.T. Dinh, T. T. Zhuang, L. Wang, J.Y. Howe, Y. Ren, E.H. Sargent, D. Sinton, Constraining CO coverage on copper promotes high-efficiency ethylene electroproduction, Nat. Catal. 2 (2019) 1124–1131.
[61] Y.C. Tan, K.B. Lee, H. Song, J. Oh, Modulating local CO_2 concentration as a general strategy for enhancing C-C coupling in CO_2 electroreduction, Joule 4 (2020) 1104–1120.
[62] X. Wang, A. Xu, F. Li, S.F. Hung, D.H. Nam, C.M. Gabardo, Z. Wang, Y. Xu, A. Ozden, A.S. Rasouli, A.H. Ip, D. Sinton, E.H. Sargent, Efficient methane electrosynthesis enabled by tuning local CO_2 availability, J. Am. Chem. Soc. 142 (2020) 3525–3531.
[63] M. Shen, L. Ji, D. Cheng, Z. Wang, Q. Xue, S. Feng, Y. Luo, S. Chen, J. Wang, H. Zheng, X. Wang, P. Sautet, J. Zhu, Hierarchical design enables sufficient activated CO_2 for efficient electrolysis of bicarbonate to CO, Joule 8 (2024) 1999–2015.
[64] P. Yue, Q. Fu, J. Li, L. Zhang, D. Ye, X. Zhu, Q. Liao, Microenvironment regulation strategies facilitating High-efficiency CO_2 electrolysis in a zero-gap bipolar membrane electrolyzer, ACS Appl. Mater. Interfaces 15 (2023) 53429–53435.